A 3D steady-state model of a tendon-driven continuum soft manipulator inspired by the octopus arm

F Renda[1], M Cianchetti, M Giorelli, A Arienti and C Laschi

The BioRobotics Institute, Scuola Superiore Sant'Anna, Viale Rinaldo Piaggio 34, 56025 Pontedera (Pisa), Italy

E-mail: f.renda@sssup.it

Abstract
Control and modelling of continuum robots are challenging tasks for robotic researchers. Most works on modelling are limited to piecewise constant curvature. In many cases they neglect to model the actuators or avoid a continuum approach. In particular, in the latter case this leads to a complex model hardly implemented. In this work, a geometrically exact steady-state model of a tendon-driven manipulator inspired by the octopus arm is presented. It takes a continuum approach, fast enough to be implemented in the control law, and includes a model of the actuation system. The model was experimentally validated and the results are reported. In conclusion, the model presented can be used as a tool for mechanical design of continuum tendon-driven manipulators, for planning control strategies or as internal model in an embedded system.

(Some figures may appear in colour only in the online journal)

1. Introduction

The effort to enhance the performance of robot manipulators has resulted in an increased attention towards continuum soft manipulators and in particular towards 'biologically inspired' soft manipulators [1, 2]. A continuum soft manipulator can be thought as a (continuous) bending robot composed of elastic elements with ideally infinite degrees of freedom (d.o.f.). They pertain to the class of hyper-redundant manipulators, which consists of a large number of short rigid links, but go beyond them by virtue of their infinite degrees of freedom [3]. Continuum soft robots have been inspired by biological systems, for example elephant trunks [4, 5], cephalopod arms [2] and mammalian tongues, which are commonly known as muscular hydrostats (for more details on the octopus arm muscular hydrostat structure see [6]).

The control and modelling of continuum manipulators are not trivial tasks because they require a continuum approach and present several degrees of nonlinearity both on the material and geometrical side. Nowadays many researchers are involved in this stimulating challenge, but the problem is yet far from being solved. Most of the approaches currently in use are limited to piecewise-constant-curvature approximation [7, 8] or they are restricted to the kinematic analysis [9]. Recently Jones and Gray [10] presented a steady-state model of a continuous robot but they did not model the actuation acting on it. In the elegant work of Boyer and Porez [11] the distributed force and torque acting on the robot are estimated but no discussion is given on the actuators that could generate them. Zheng and Branson [12] developed a model based on a spring-mass approach instead of a continuum one that is too complex to be implemented in an embedded system. Exact solutions also exist [13] but, in any case, the bottle neck in their use is the real time implementation of the model due to the computational effort required. This suggests the necessity of smart simplifications.

In this work, a 3D geometrically exact steady-state model of a continuum manipulator inspired by the octopus arm, driven by tendons, is presented. With respect to the state of the art, in this work both robot body and actuators have been modelled and the developed continuum approach is fast

---

[1] Author to whom any correspondence should be addressed.
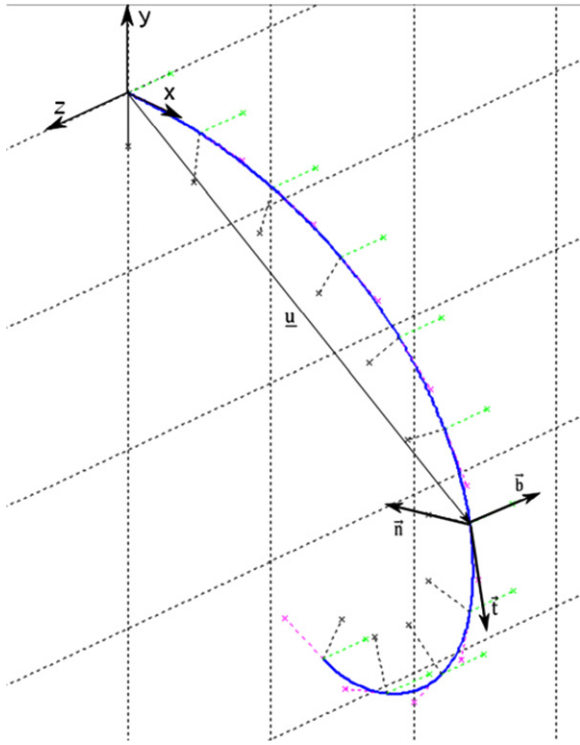
Figure 1. Cosserat beam kinematics. The material element is identified by a position vector $\underline{u}$ and a local reference frame $\vec{t}, \vec{n}, \vec{b}$.

enough to be implemented in the embedded control of the manipulator. Thanks to its generality, this model can also be used as a powerful virtual platform for testing a number of design parameters.

The rest of the paper is divided into six sections. In section 2, the mathematical framework of the model is described, both for the kinematic and static problems. In section 3, the mechanical design of the octopus-inspired robot arm is described and section 4 is focused on showing how the 3D steady-state model has been derived. In section 5, the model has been validated through several tests on a real prototype and the potentialities of the model are shown through specific results in section 6. Section 7 is dedicated to the conclusions.

2. Mathematical framework

The idea is to model a continuum manipulator (composed of a single piece of silicone) as a slender Cosserat beam. In the following subsections the kinematic and static models (chosen for this work) of such a rod are described.

2.1. Kinematics

A Cosserat beam is a one-dimensional continuum body in which the generic material element is considered as a (infinitesimally small) *rigid body* which can rotate independently of the neighbouring fellows [14]. In order to describe this rotation every material element is represented by a tern of directors. Two of them ($\vec{n}$ and $\vec{b}$) lie on the cross-section plane and the third, perpendicular to the plane, comes out in the direction of the tip of the beam ($\vec{t}$) (figure 1). Furthermore, as in other beam theories, the material element carries the
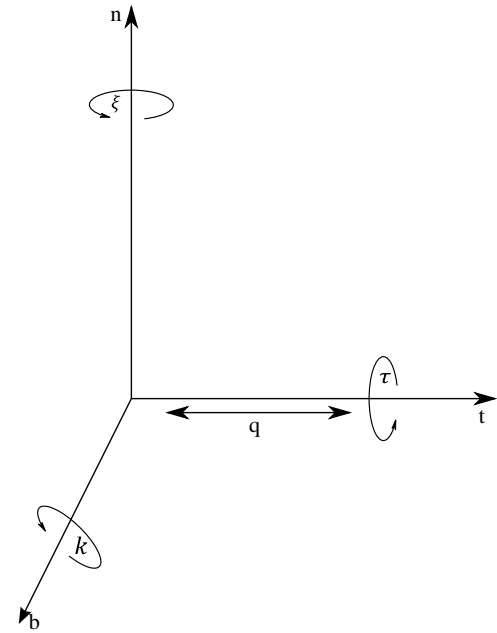
Figure 2. D.o.f of one cross section.

material properties and the geometrical properties of the cross section. For this reason, in the remainder of the paper we will directly call the material element the cross section. For all the local reference frames $\vec{t} \times \vec{n} = \vec{b}$ holds. The geometric transformation between two consecutive local frames is determined by the strain values of the section itself; thus we could reconstruct the shape of the beam, after referring it to a fixed frame, by knowing the strain quantities along the beam and the position and orientation of the base local frame. In fact the deformation of the beam is the continuous infinitesimal homologous of the usual internal joint (d.o.f.) of a serial manipulator. In the following let us call the deformations of the robot arm d.o.f., which is more suitable in the robotic field.

In the classical theory, the d.o.f. of one section are six [14]: the curvatures along the two axes lying on the section plane, the torsion on the third perpendicular axis, two shear strains and the longitudinal strain. We assume the shear strains to be negligible; therefore in our case each section of the beam has four d.o.f. In other words, the Euler–Bernoulli hypothesis has been adopted. In this case the perpendicular axis of the section is parallel to the tangent vector of the beam backbone. Let us call $\underline{\underline{t}}$ the matrix of the local reference frame $(\vec{t}, \vec{n}, \vec{b})^T$ expressed in a fixed frame lying at the base of the beam (figure 1), s the material arc length along the reference configuration of the manipulator and S the spatial arc length on the actual configuration. We know from the literature [15] the push forward transformation of $\underline{\underline{t}}$ with respect to S: $d\underline{\underline{t}}/dS = (\hat{\underline{\omega}})^T \underline{\underline{t}}$, where $\hat{\underline{\omega}}$ is the skew-symmetric tensor of $\underline{\omega} = (\tau, \xi, k)$, that is the vector of the three rotational d.o.f. expressed in the local reference frame. k and ξ represent respectively the curvature with respect to the axes $\vec{b}$ and $\vec{n}$, and τ represents the torsion of the section with respect to the axis $\vec{t}$ (figure 2).

Thanks to the Euler–Bernoulli hypothesis we have $d\underline{\underline{t}}/ds = d\underline{\underline{t}}/dS * dS/ds = (\hat{\underline{\omega}})^T \underline{\underline{t}} \operatorname{diag}(1 + q)$. In the same

way we have $\mathrm{d}\underline{u}/\mathrm{d}s = (1+q)\vec{t}$, where $\underline{u}$ is the position vector of the centre of mass of the section identified by the variable s expressed in the fixed frame (figure 1) and q is the longitudinal strain (figure 2). The following expressions (1) show the kinematic equations of our Cosserat beam in an 'expanded' and friendlier version:

$$
\begin{aligned}
\frac{\mathrm{d}}{\mathrm{d}s}\left(\vec{t}\right) &= k\,(1+q)\,\vec{n} - \xi\,(1+q)\,\vec{b}, \\
\frac{\mathrm{d}}{\mathrm{d}s}\left(\vec{n}\right) &= -k\,(1+q)\,\vec{t} + \tau\,(1+q)\,\vec{b}, \\
\frac{\mathrm{d}}{\mathrm{d}s}\left(\vec{b}\right) &= \xi\,(1+q)\,\vec{t} - \tau\,(1+q)\,\vec{n}, \\
\frac{\mathrm{d}}{\mathrm{d}s}\left(\underline{u}\right) &= (1+q)\,\vec{t}.
\end{aligned}
\tag{1}
$$

Those d.o.f. correspond to the joint space of a classical serial manipulator; thus the Euler–Bernoulli simplification simplifies not only the model but also the control strategy and it favours its implementation on an embedded system.

2.2. Statics

The motion of a beam is described by the equilibrium and constitutive equations. The following expressions (2) show the equilibrium equations (under the steady-state condition) derived by Simo and Vu-Quoc in their fundamental works on a geometrically exact Cosserat beam [16–18]:

$$
\begin{aligned}
\frac{\mathrm{d}}{\mathrm{d}s}\left(\underline{F}\right) + \underline{n} &= 0, \\
\frac{\mathrm{d}}{\mathrm{d}s}\left(\underline{M}\right) + \frac{\mathrm{d}}{\mathrm{d}s}\left(\underline{u}\right) \times \underline{F} + \underline{m} &= 0,
\end{aligned}
\tag{2}
$$

where $\underline{F}$ is the vector of the internal contact force and $\underline{M}$ is the vector of the internal torque force. $\underline{n}$ and $\underline{m}$ are respectively the external applied force and torque for unit of reference length. Everything is expressed in the local reference frame.

We assume the beam to be made of a hyper-elastic material and the constitutive equations to be linear ((3a), (3b)):

$$
\begin{pmatrix} GI & 0 & 0 \\ 0 & EJ_n & 0 \\ 0 & 0 & EJ_b \end{pmatrix}
\begin{pmatrix} \tau(s) \\ \xi(s) \\ k(s) \end{pmatrix} = \underline{M}(s),
\tag{3a}
$$

$$
EAq(s) = N(s).
\tag{3b}
$$

N is the $\vec{t}$ component of $\underline{F}$, E is the Young modulus, G is the shear modulus, I, J_n and J_b are respectively the moment of inertia of the section with respect to axes $\vec{t}, \vec{n}$ and $\vec{b}$. We assume that both the cross section and the constitutive equations do not change with the deformation.

The rotational d.o.f. has been considered to belong to C^1 class function; thus we can derive equation (3a) obtaining the following expression:

$$
\begin{aligned}
&\begin{pmatrix} GI & 0 & 0 \\ 0 & EJ_n & 0 \\ 0 & 0 & EJ_b \end{pmatrix}
\begin{pmatrix} \frac{\mathrm{d}}{\mathrm{d}s}\tau \\ \frac{\mathrm{d}}{\mathrm{d}s}\xi \\ \frac{\mathrm{d}}{\mathrm{d}s}k \end{pmatrix}
+ \begin{pmatrix} G\dot{I} & 0 & 0 \\ 0 & E\dot{J}_n & 0 \\ 0 & 0 & E\dot{J}_b \end{pmatrix} \\
&\times \begin{pmatrix} \tau(s) \\ \xi(s) \\ k(s) \end{pmatrix} = \underline{\dot{M}}(s),
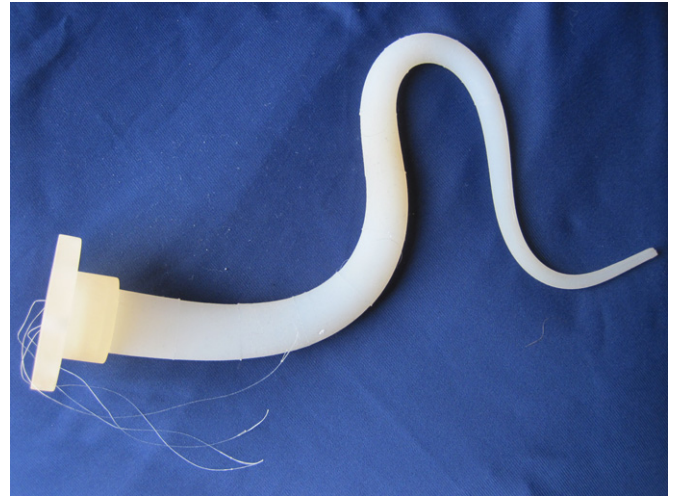\end{aligned}
\tag{4}
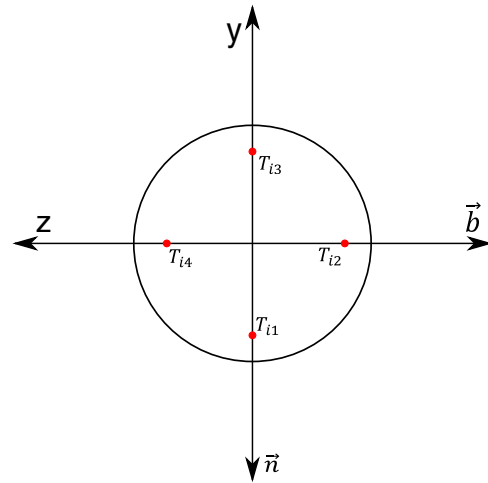$$

Figure 3. Octopus-like arm prototype.

Figure 4. Transversal section of a robot arm anchorage cross section in the reference configuration. The figure shows the relative position of the four cables indicated with the symbols T_{i1}, T_{i2}, T_{i3} and T_{i4}.

where the dot means the derivative with respect to s. For our problem it is useful to solve equation (4) instead of equation (3a) as shown in the following sections.

3. Octopus-inspired robot arm

In this section the octopus-inspired robot arm is described (figure 3).

The robot arm is composed of a single conical piece of silicone (that represents our Cosserat beam) actuated by several cables immersed inside the body and anchored at different distances from the base through a rigid plastic disc built in the robot arm. Such discs are embedded in the silicone during the fabrication process and they can be placed in any position inside the arm. There are four cables for each anchorage cross section aligned with the axes $\vec{n}$ and $\vec{b}$ as shown in figure 4 (for more detail on the design of such a prototype see [19, 20]). By pulling one cable the robot arm bends on the side of the cable in a way that depends on the cable tension and on the
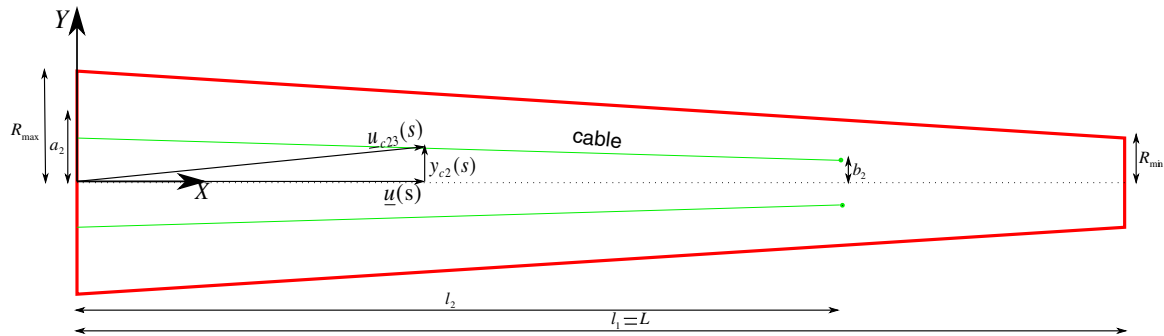
Figure 5. Tendon position inside the body of the robot arm. R_{max} and R_{min} are respectively the radius of the base and of the tip; $\underline{u}(s)$ is the position vector of the material element; $y_{ci}(s)$ is the distance from the cables to the midline; $\underline{u}_{c23}(s)$ is the position vector of the third cable fastened at the second anchorage cross section; a_2 and b_2 are respectively the distance at base and at anchorage level of the cables fastened at the second anchorage cross section with length l_2; L is the total length of the manipulator, equal to l_1 in this paper. To enhance the clarity of the representation, the cables of sections 1 and 3 are hidden.

arrangement of the tendon inside the robot body. In this way the manipulator can be bent and twisted 'arbitrarily' in 3D space by pulling several cables anchored at different distances from the base. The anchorage sites have been labelled with the corresponding cross sections s using the subscript i to number them beginning from the tip of the robot arm. In particular, in this paper a robot arm with three anchorage cross sections has been analysed.

The tendons are coated by a polymer sheath to avoid friction generated by the direct contact between the cable and the silicone body of the robot.

The robot arm works in water, to exploit the mechanical properties of the material and the interaction with the environment.

The path of the cables inside the body is linear with respect to s (5). All the tendons that are attached at the same cross section have the same distance to the midline. Let us call $y_{ci}(s)$ the distance of the cables attached to the ith anchorage section from the midline (figure 5), which is simply

$$y_{ci} = \left(\frac{b_i - a_i}{l_i} \right) s + a_i, \qquad (5)$$

where a_i and b_i are respectively the distance of the tendon from the midline at base level and at anchorage level and l_i is the value of s relative to the anchorage cross section i (figure 5). The kinematics of the robot arm and function $y_{ci}(s)$ determine the kinematics of the cables as follows:

$$
\begin{aligned}
\underline{u}_{ci1}(s) &= \underline{u}(s) + y_{ci}\vec{n}, \\
\underline{u}_{ci2}(s) &= \underline{u}(s) + y_{ci}\vec{b}, \\
\underline{u}_{ci3}(s) &= \underline{u}(s) - y_{ci}\vec{n}, \\
\underline{u}_{ci4}(s) &= \underline{u}(s) - y_{ci}\vec{b}.
\end{aligned}
\qquad (6)
$$

We add a subscript c for all the kinematic quantities relative to the tendons. We call $R(s)$ the radius of the section s. Since the manipulator has a conical shape it is linear with respect to s, as shown in (7), where L is the total length of the robot arm, R_{max} and R_{min} are respectively the radius of the base and of the tip anchorage cross sections:

$$R = \left(\frac{R_{min} - R_{max}}{L} \right) s + R_{max}. \qquad (7)$$

Note that L is equal to l_1 if the cables are fixed to the tip as in this paper.

The manipulator has a circular cross section; therefore $J_n(s)$ and $J_b(s)$ are the same and equal to $\pi R(s)^4/4$. The torsion moment of inertia I is equal to $\pi R(s)^4/2$ and the area A is equal to $\pi R(s)^2$. The shear modulus G can be calculated with $E/2(1+\upsilon)$ where υ is the Poisson ratio.

4. 3D steady-state model of the octopus-inspired robot arm

In this section the 3D steady-state model is derived, followed by a discussion on the computational aspect of the numerical solution.

The force and torque acting on the robot arm are due to the tension of the cables, gravity and buoyancy (under a steady-state condition). In our model we consider only the first one because the others require a more complex solution algorithm that we are going to develop directly for the full dynamic case. Furthermore the robot arm has been designed such that the buoyancy and gravity are almost complementary, as the density of silicone is very close to the density of water. The remaining force could be eventually eliminated by applying floats on the arm.

Let us consider the robot arm stuck at the base to the frame; then the cables allow a point load located where the cables are fastened, equal to the cable tension and tangent to it $-T\vec{t_c}(l_i)$ (i.e. the classical tendon transmitted load) and a distributed load along the cable configuration, due to the contact between the cable and the robot arm silicone body. Since we neglect the friction, the contact force is orthogonal to the cable (centripetal) and equal to $T\mathrm{d}\vec{t_c}/\mathrm{d}S_c$ (figure 6), where S_c represents the arc-length parameterization of the cable. In other words we assume the tendon to be a pure tension element. For a detailed mechanical analysis of this tendon load see the fundamental work of Camarillo *et al* [8].

Since the tendons are immersed inside the body, the static problem is a following force problem.

4
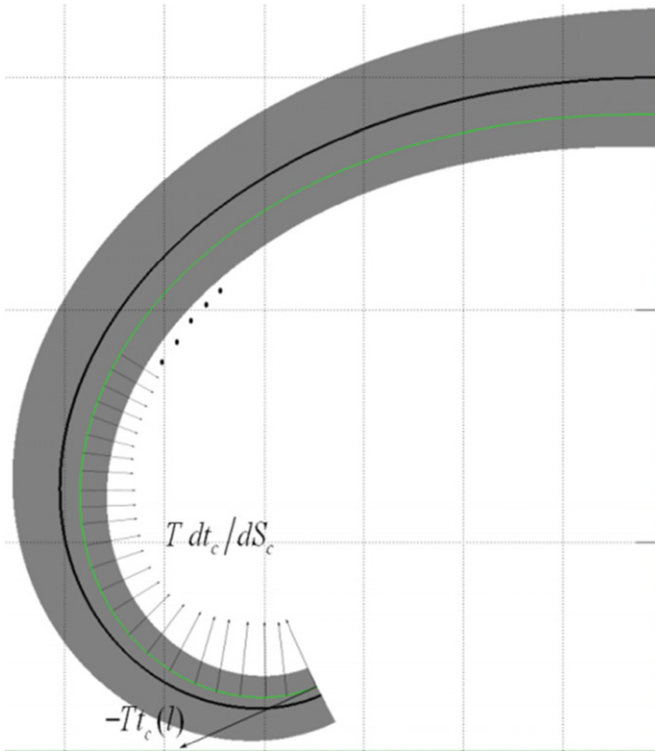
Figure 6. Distributed and point load acting on the manipulator due to cable tension. The latter is the classical tendon transmitted force and the former is the contact force between the cable and the silicone robot body. Since there is no friction, the contact force is orthogonal to the cable (centripetal).

Given the loads of figure 6, the equilibrium equations of our manipulator are

$$\underline{M}_{ij}(s) = -T_{ij}\vec{t}_{cij}(l_i) \times (\underline{u}(s) - \underline{u}_{cij}(l_i)) + \int_s^l T_{ij}\frac{\mathrm{d}\vec{t}_{cij}}{\mathrm{d}\eta}$$
$$\times (\underline{u}(s) - \underline{u}_{cij}(\eta))\,\mathrm{d}\eta, \tag{8a}$$

$$N_{ij}(s) = -T_{ij}\vec{t}_{cij}(l_i) \cdot \vec{t}(s) + \vec{t}(s) \cdot \int_s^l T_{ij}\frac{\mathrm{d}\vec{t}_{cij}}{\mathrm{d}\eta}\,\mathrm{d}\eta, \tag{8b}$$

where $j \in \{1, 2, 3, 4\}$ identifies one of the four cables of the anchorage section i; therefore the subscript ij identifies univocally one tendon. Note that to deduce the equations in (8) the following equivalence has been used: $\frac{\mathrm{d}\vec{t}_c}{\mathrm{d}S_c} \times (...)\mathrm{d}S_c = \frac{\mathrm{d}\vec{t}_c}{\mathrm{d}\eta}\frac{\mathrm{d}\eta}{\mathrm{d}S_c} \times (...)\frac{\mathrm{d}S_c}{\mathrm{d}\eta}\mathrm{d}\eta = \frac{\mathrm{d}\vec{t}_c}{\mathrm{d}\eta} \times (...)\mathrm{d}\eta$.

By deriving equation (8a) and developing the integrals we obtain the expressions of N_{ij} and $\dot{M}_{ij}$ as follows:

$$N_{ij}(s) = -T_{ij}\vec{t}_{cij} \cdot \vec{t}, \tag{9a}$$

$$\dot{\underline{M}}_{ij}(s) = -T_{ij}\vec{t}_{cij} \times \vec{t} - T_{ij}\frac{\mathrm{d}\vec{t}_{cij}}{\mathrm{d}s} \times (\underline{u} - \underline{u}_{cij}). \tag{9b}$$

$\vec{t}_{cij}$ is equal to $\mathrm{d}\underline{u}_{cij}/\mathrm{d}s$, where we have assumed s to be a good approximation of the arc-length parameterization of the cables (S_c) and of the midline (S). $\underline{u}_{cij}$ is defined in the equations in (6). Finally, once we have developed the products, the equations (9) represent the stress contribution of one cable ij.

The equation in (9b) can be easily expressed in terms of the local frame contrary to M_{ij} (8a). This is the reason why we

do not use directly the equation of M_{ij} to solve the equation in (3a).

The internal stresses of equations (3b) and (4) are defined as follows: $N(s) = \sum_{i,j=1}^{n,4} N_{ij}(s)$ and $\underline{\dot{M}}(s) = \sum_{i,j=1}^{n,4} \dot{\underline{M}}_{ij}(s)$, where $n \in \aleph$ in the interval $[1, n_{\max}]$ and represents the number of anchorage cross sections which are from the section s to the tip of the robot arm and $n_{\max}$ is the total number of anchorage cross sections (three for our prototype). It follows that the behaviour of $N(s)$ and $\dot{M}(s)$ has a point of discontinuity for every value of s corresponding to an anchorage cross section. Finally, handling the constitutive equations (3b) and (4) the characteristic differential equations of the d.o.f. of the manipulator have been obtained:

$$\frac{\mathrm{d}}{\mathrm{d}s}\tau = -\tau\frac{G\dot{I} + \sum_{i=1}^n \left(2y_{ci}\dot{y}_{ci}\sum_{j=1}^4 T_{ij}\right)}{GI + \sum_{i=1}^n \left(y_{ci}^2\sum_{j=1}^4 T_{ij}\right)}$$
$$- k\xi\frac{\sum_{i=1}^n \left(y_{ci}^2(T_{i1} - T_{i2} + T_{i3} - T_{i4})\right)}{GI + \sum_{i=1}^n \left(y_{ci}^2\sum_{j=1}^4 T_{ij}\right)}$$
$$+ k\frac{\sum_{i=1}^n \left(y_{ci}(T_{i2} - T_{i4})\right)}{GI + \sum_{i=1}^n \left(y_{ci}^2\sum_{j=1}^4 T_{ij}\right)}$$
$$+ \xi\frac{\sum_{i=1}^n \left(y_{ci}(T_{i1} - T_{i3})\right)}{GI + \sum_{i=1}^n \left(y_{ci}^2\sum_{j=1}^4 T_{ij}\right)},$$

$$\frac{\mathrm{d}}{\mathrm{d}s}\xi = -\xi\frac{E\dot{J} + \sum_{i=1}^n \left(2y_{ci}\dot{y}_{ci}(T_{i2} + T_{i4})\right)}{EJ + \sum_{i=1}^n \left(y_{ci}^2(T_{i2} + T_{i4})\right)}$$
$$- \tau k\frac{\sum_{i=1}^n \left(y_{ci}^2(T_{i2} + T_{i4})\right)}{EJ + \sum_{i=1}^n \left(y_{ci}^2(T_{i2} + T_{i4})\right)}$$
$$+ \tau\frac{\sum_{i=1}^n \left(y_{ci}(T_{i3} - T_{i1})\right)}{EJ + \sum_{i=1}^n \left(y_{ci}^2(T_{i2} + T_{i4})\right)}$$
$$+ \frac{\sum_{i=1}^n \left(\dot{y}_{ci}(T_{i4} - T_{i2})\right)}{EJ + \sum_{i=1}^n \left(y_{ci}^2(T_{i2} + T_{i4})\right)},$$

$$\frac{\mathrm{d}}{\mathrm{d}s}k = -k\frac{E\dot{J} + \sum_{i=1}^n \left(2y_{ci}\dot{y}_{ci}(T_{i3} + T_{i1})\right)}{EJ + \sum_{i=1}^n \left(y_{ci}^2(T_{i3} + T_{i1})\right)}$$
$$+ \tau\xi\frac{\sum_{i=1}^n \left(y_{ci}^2(T_{i3} + T_{i1})\right)}{EJ + \sum_{i=1}^n \left(y_{ci}^2(T_{i3} + T_{i1})\right)}$$
$$+ \tau\frac{\sum_{i=1}^n \left(y_{ci}(T_{i4} - T_{i2})\right)}{EJ + \sum_{i=1}^n \left(y_{ci}^2(T_{i3} + T_{i1})\right)}$$
$$+ \frac{\sum_{i=1}^n \left(\dot{y}_{ci}(T_{i1} - T_{i3})\right)}{EJ + \sum_{i=1}^n \left(y_{ci}^2(T_{i3} + T_{i1})\right)},$$

$$q = \frac{\sum_{i=1}^n \left[ky_{ci}(T_{i1} - T_{i3}) + \xi y_{ci}(T_{i4} - T_{i2}) - \sum_{j=1}^4 T_{ij}\right]}{EA}. \tag{10}$$

The equations in (10) have to be integrated with (5) and (7), missing nothing but the geometrical parameters and the values of the cable tensions (both arbitrarily chosen). Thanks to its generality, the model expressed in the equations in (10) could be used as a powerful design tool for many kinds of slender continuum manipulators driven by tendons. The longitudinal strain q is a function of k and ξ; thus it can be calculated in one step once we obtain them. The last equation in (10), indeed, is not a differential equation.
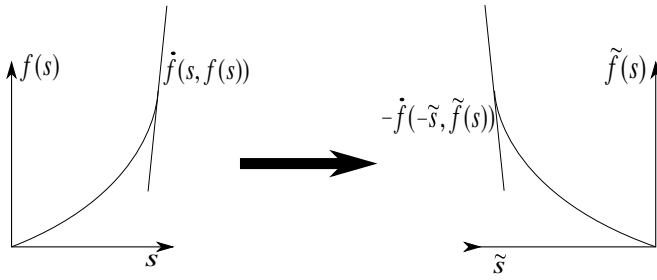
Figure 7. Graphical example of transformation (12) from a final value problem for differential equation (left) to an initial value problem for differential equation (right).

The equations in (10) embed the same points of discontinuity along the domain of *s* because the expressions of $N(s)$ and $\underline{\dot{M}}(s)$ change dramatically immediately before and after an anchorage cross section. What changes is the number of cables acting on the section that is represented by the index *n*. Therefore we use one set of equations for each interval between two anchorage cross sections each with a different value of *n*. The *i*th equation set is defined in the semi-open domain $(l_{i+1}, l_i]$ except the last one (recall that we begin to enumerate from the tip of the robot arm) which is defined in the interval $[0, l_{n_{max}}]$.

Since the robot arm is stuck to the frame at the base we have the so-called kinematic boundary condition at $s = 0$ (i.e. $\underline{u}(0)$, $\vec{t}(0)$, $\vec{n}(0)$ and $\vec{b}(0)$) and static boundary condition at

$s = L = l_1$ ($\tau(l_1)$, $\xi(l_1)$, $k(l_1)$ and $q(l_1)$). Therefore the idea is to integrate the equations in (10) beginning from the tip of the robot arm to obtain the expression for the robot arm d.o.f. and afterwards to integrate the kinematic equations (1) to obtain the arm shape. The boundary condition for the *i*th internal set of equations at $s = l_i$ (equations in (11)) is composed of the contribution of the cables fixed at the anchorage cross section *i* and of the solutions at $s = l_i^+$ of the $(i - 1)$th ordinary differential equation (ODE) where the apex + indicates the positive limit. The first contribution is derived calculating $\underline{M}$ using equation (3*a*):

$$\begin{aligned} \tau(l_i) &= \tau(l_i)^+, \\ \xi(l_i) &= \frac{b_i(T_{i4} - T_{i2})}{b_i^2(T_{i4} + T_{i2}) + EJ} + \xi(l_i)^+, \\ k(l_i) &= \frac{b_i(T_{i1} - T_{i3})}{b_i^2(T_{i1} + T_{i3}) + EJ} + k(l_i)^+. \end{aligned} \tag{11}$$

From a mathematical point of view every set of equations (10) and (11) is a final value problem for ordinary differential equations. For our purposes we integrate them numerically as shown in the following section.

4.1. Computational aspect

Some modifications have to be applied on the equations in (10) and their domain to be numerically integrated by an ODE solver. In particular, the following are obtained:
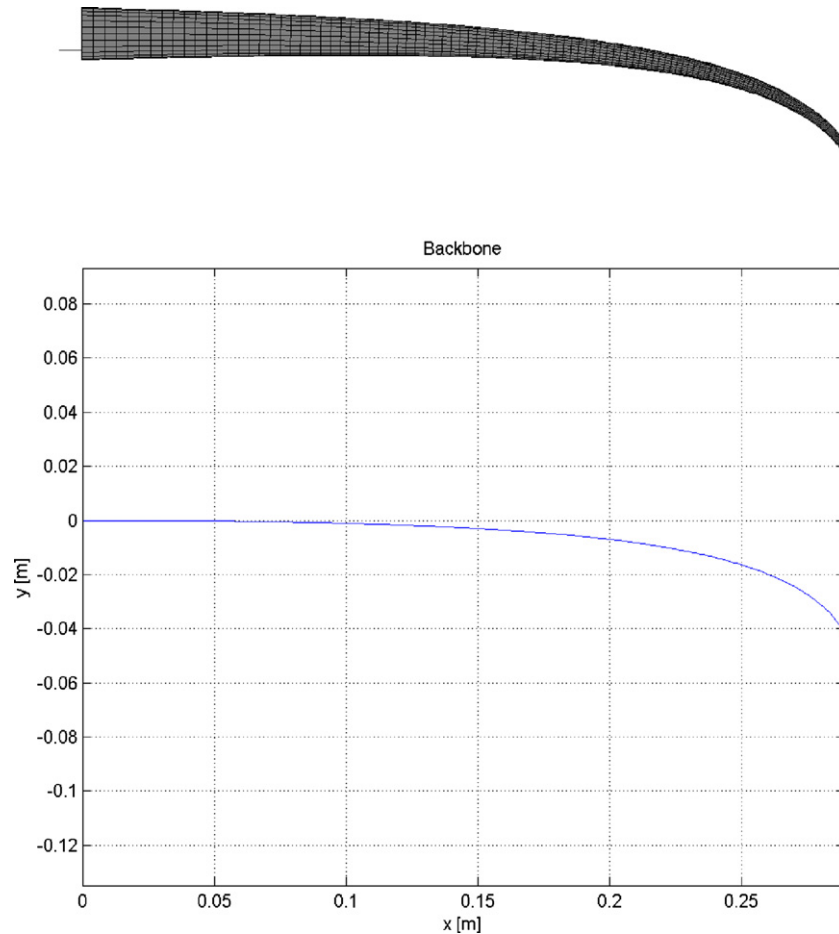
Figure 8. FEM model (top) and analytical model (bottom) with the same parameters: the two models behave in a very similar manner.
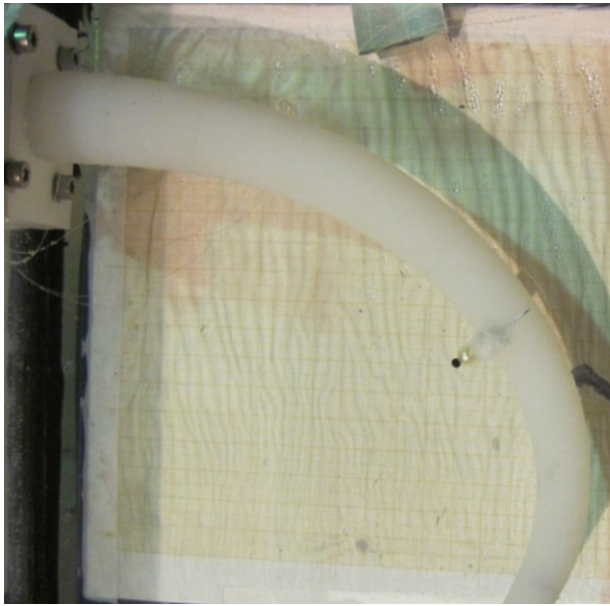
Figure 9. The comparison between the real silicone arm and the model highlights a very small difference on the midline configuration.
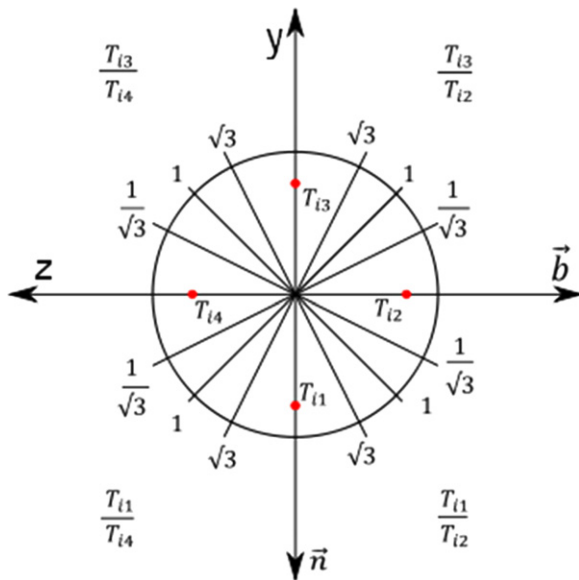
Figure 10. Several bending planes and relative cable tension ratio.

Table 1. Tip error between the analytical model and the real prototype under different tension conditions.

T (N)	$\Delta \underline{u}(L)/L$ (%)
0.53	3.0
1.09	5.5
2.00	3.5
2.60	6.7
3.06	7.8
3.44	7
3.95	4.8
Average	5.4

$$\tilde{s} = -s,$$
$$\tilde{\underline{\omega}}(\tilde{s}) = \underline{\omega}(s),$$
$$\frac{\mathrm{d}}{\mathrm{d}s}\tilde{\underline{\omega}}(\tilde{s}, \tilde{\underline{\omega}}) = -\frac{\mathrm{d}}{\mathrm{d}s}\underline{\omega}(-s, \underline{\omega}). \tag{12}$$

Table 2. Model parameters (all lengths are in (mm)).

E (kPa)	υ	$L = l_1$	$R_{\min}$	$R_{\max}$	b_1	a_1	b_2	a_2	l_2	b_3	a_3	l_3
110	0.5	310	6.5	15	1	7.5	3.5	3.5	217	6	6	93

Table 3. Tension of the tendons associated with the relative results (not reported cables are set to zero).

	T_{11} (N)	T_{12} (N)	T_{13} (N)	T_{14} (N)
Figure 11(*a*)	0	0	1	1
Figure 11(*b*)	1	$\sqrt{3}$	0	0
Figure 11(*c*)	0	1	$\sqrt{3}$	0

Table 4. Model parameters (all lengths are in (mm)).

| E (kPa)	υ	$L = l_1$	$R_{\min}$	$R_{\max}$	b_1	a_1	b_2	a_2	l_2	b_3	a_3	l_3
110	0.5	450	2	15	1	7.5	3.5	3.5	315	6	6	135

Table 5. Tension of tendons both for two-dimensional and three-dimensional fetching (not reported cables are set to zero).

	T_{13} (N)	T_{21} (N)	T_{33} (N)	T_{32} (N)
Figure 14	0.5	4	13	0
Figure 15	0.5	4	0	13

Applying substitutions (12) in (10) and (11) (note that they also influence (5) and (7)) we obtain a set of initial value problem for ordinary differential equation in the variable $\tilde{s}$ and the unknown $\tilde{\underline{\omega}}(\tilde{s})$, that can be solved in MatLab® (MatLab® 2009a, The Mathworks Inc., Natick, MA) using an appropriate ODE function (for example *ode23*). Figure 7 illustrates the meaning of the transformation (12).
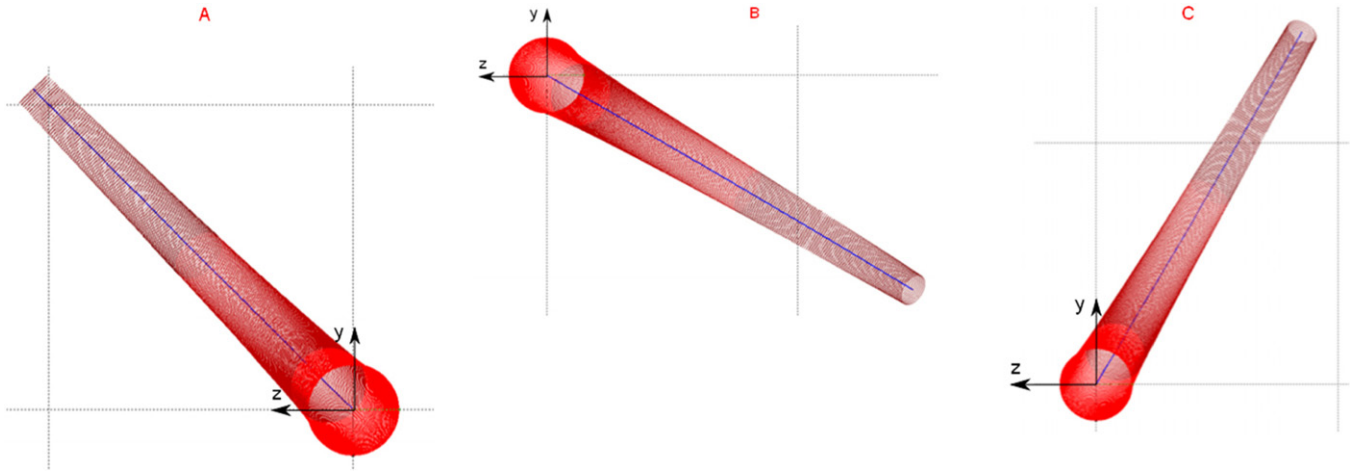
Figure 11. Three different planes of bending: (*A*) 135°; (*B*) −30°; (*C*) 60°.
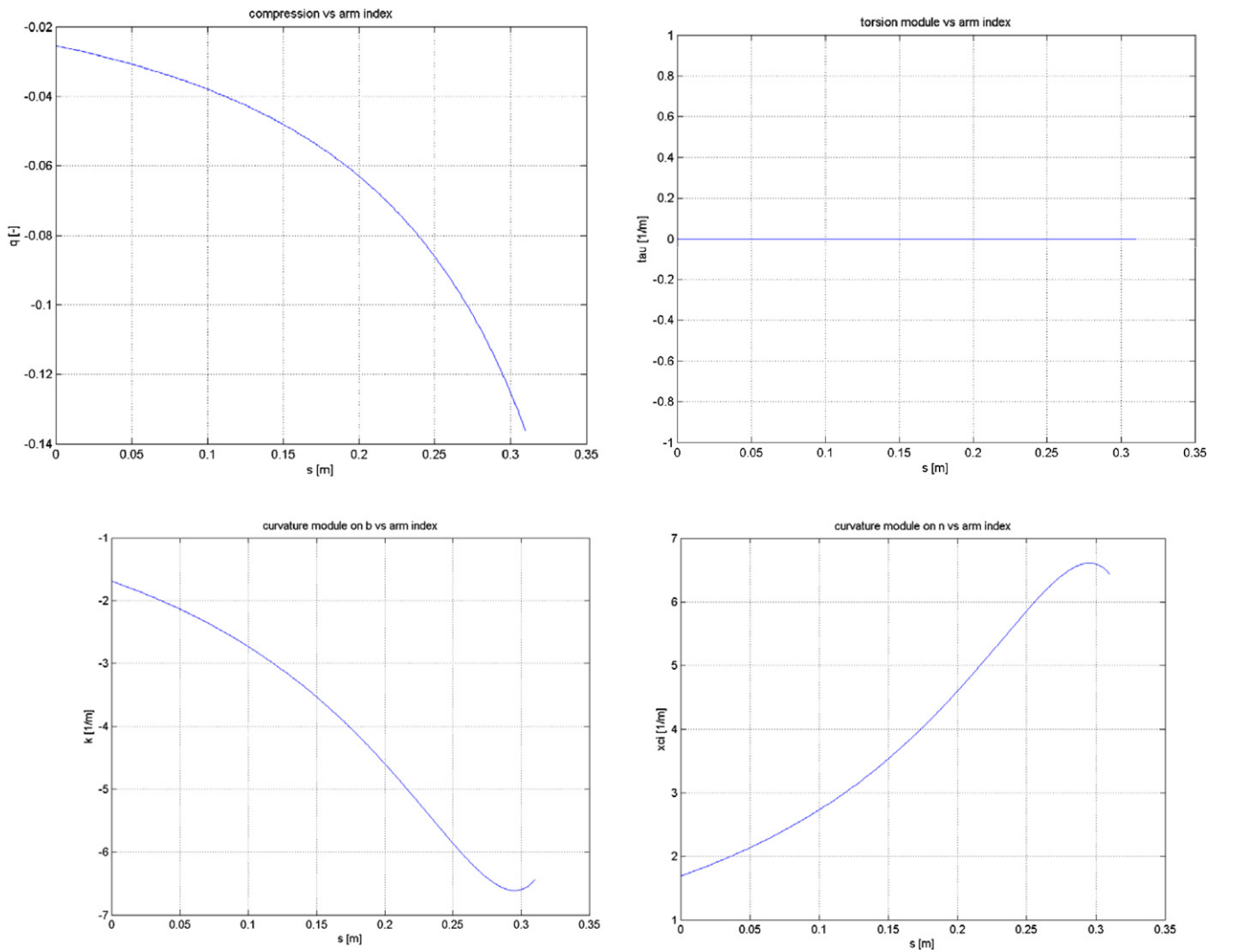

Figure 12. Trend of the d.o.f of the manipulator along the arm in the case of figure 11(*a*).

Afterwards a pullback transformation has to be performed just by applying the first and the second equations in (12) to the results.

The kinematic equations in (1) are solved directly with MatLab® once we obtain the functions $\tau(s)$, $\xi(s)$, $k(s)$ and $q(s)$, starting from any desired initial condition of $\underline{u}$, $\vec{t}$, $\vec{n}$ and
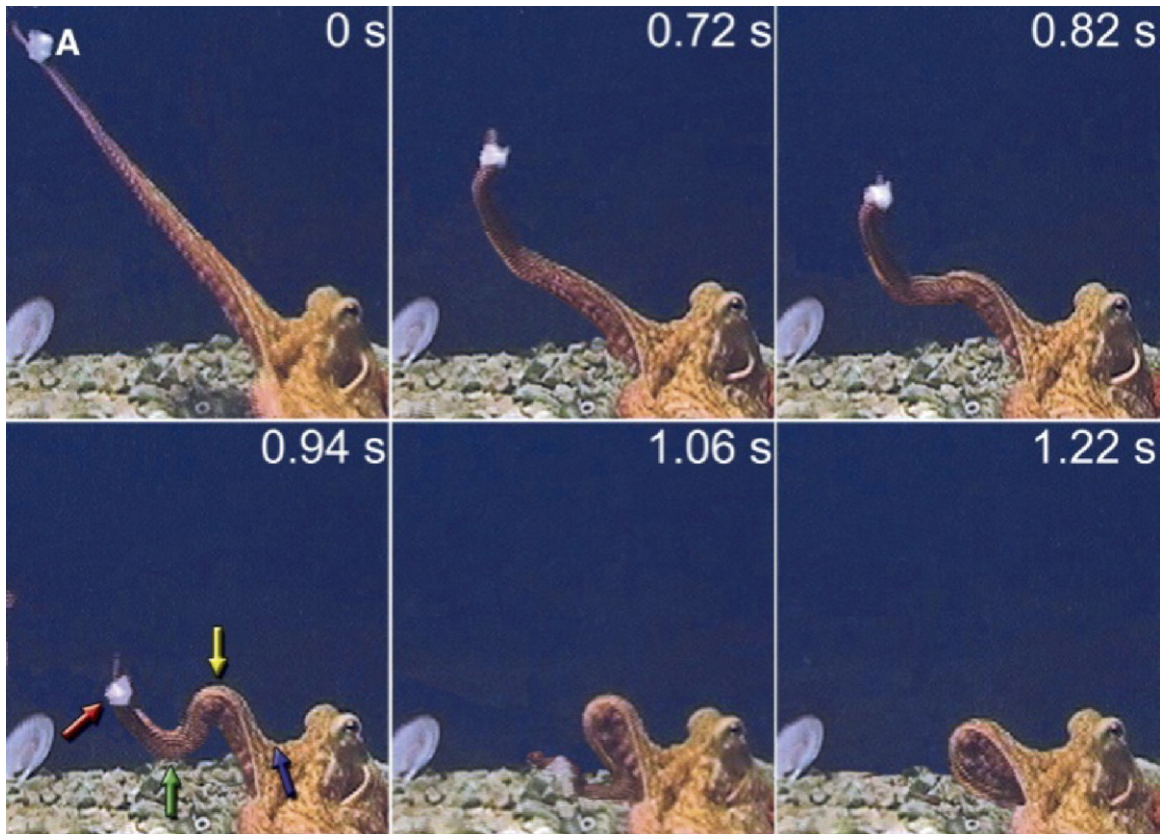
Figure 13. Octopus fetching movement composed of three bends: proximal, medial and distal (reproduced with the permission of the author and publisher of [21]).
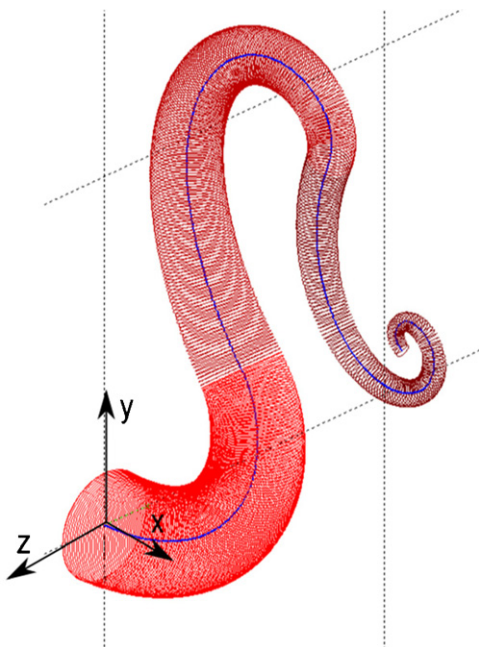
Figure 14. Simulated fetching in one plane.

$\vec{b}$ that corresponds to the position and orientation of the base of the manipulator.

5. Validation of the model

To corroborate the above model a procedure divided into two steps has been followed.

5.1. Analytical versus FEM model

First of all a FEM model (on MARC®/Mentat® 2010, MSC Software) with the same parameters (see below) of the analytical model has been used to validate the algebraic correctness of the equations.

The silicone arm has been modelled using HEX elements with Herrmann formulation (known to be better performing for highly deformable materials) while the cable has been represented by a chain of beam elements. Since the sheath is composed of the same material as the rest of the arm, its function has been replicated with an almost cylindrical internal space left inside the silicone arm, in which the cable is lodged. In this way, the cable is free to go in and out of the arm when pulled, but the contact analysis has been activated to predict the correct distribution of the stresses when it touches the silicone and to avoid compenetration of the cable into the rest of the arm. All material and geometric properties of the real prototype have been used, but the friction between the cable and the silicone has been set to zero to meet the same assumption of the analytical model.

For these tests an arm with length L equal to 300 mm has been used, and R_{max} and R_{min} are respectively equal to 10 and
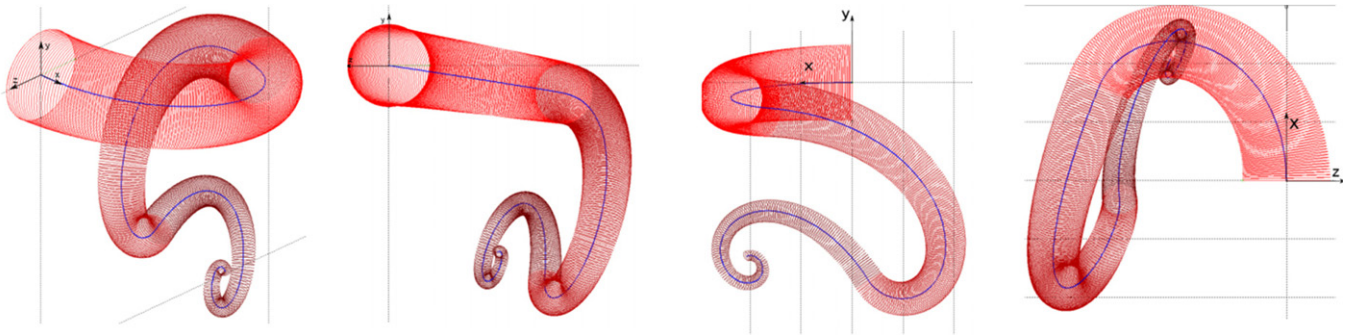
Figure 15. Different views of the three-dimensional fetching.

1.5 mm. Only one cable has been simulated with a_1 equal to 0.66 mm and b_1 equal to 1 mm. As can be seen in figure 8 an almost perfect correlation has been obtained with a maximum error detected on the tip equal to 1 mm, in the case of the same cable tension.

5.2. Analytical model versus real prototype

A silicone arm, with one cable fixed to the tip, has been built and a Plexiglas tank has been set up to measure the curvature of the real arm and compare it with the analytical model. On one side of the tank we fixed the silicone arm with the following characteristics: L is equal to 270 mm, the base radius R_{max} is 15 mm, the last anchorage section radius (the tip of the arm) R_{min} is equal to 7.4 mm, b_1 is 2.5 mm, a_1 is 5 mm and E is equal to 110 kPa (stress–strain linear approximation for compression). Finally we exerted various tensions on the cable and we took pictures of the arm by means of a camera fixed over the plane of motion. The midline was manually extrapolated and processed in MatLab® for comparison with the corresponding midlines obtained with the model.

As shown in table 1 the average error measured at the tip is less than 6% of the arm length L.

In figure 9 the real arm and the model configuration are shown in the case of 3 N tension. The error generally is higher on the distal part of the manipulator (a small error on the base results in a big error on the tip because it is integrated along the arm, see (1)). The highest errors are probably due to the nonlinearity of the material, the friction of the cables and in particular to the human error in the manual extrapolation process of the midline from the pictures.

6. Results

The results of the model actuated by several tendon tensions are shown in the following. In all the results the steady-state behaviour of a manipulator with three anchorage cross sections and four cables for each section is reproduced. The data of every simulation are collected in a summarizing table. In all the cases the orientation of the base is: $\vec{t} = (1, 0, 0)$, $\vec{n} = (0, -1, 0)$, $\vec{b} = (0, 0, -1)$, centred at $(0, 0, 0)$ (fixed frame coordinates).

It is important to remember that the considered robot arm is highly under-actuated, as we do not have an actuator for

every $(4 * \infty)$ d.o.f. Those d.o.f. are highly connected to each other by the law developed in this paper. For this reason the equations in (10) become a fundamental tool for planning control strategy.

6.1. Bending

To generate bending it is sufficient to pull one cable, but the use of different cables of the same level also allows the modulation of the plane of bending.

The results show that it is possible to select a plane of bending just by pulling two consecutive cables ($T_{i1} - T_{i2}, T_{i2} - T_{i3}, T_{i3} - T_{i4}, T_{i4} - T_{i1}$) with a specific ratio between the tensions. This ratio, in fact, corresponds to the ratio between the sine and the cosine of the desired inclination of the bending plane (figure 10). In other words the following expression holds: $\theta = \tan^{-1}(T_{i3-1}/T_{i2-4})$, where θ is the anticlockwise angle of the bending plane. Increasing the absolute value of the tension leads to a higher curvature along the arm, similarly to the case of one cable presented in the validation.

In figure 11 a few explanatory examples of those important characteristics are shown. Figure 12 illustrates in particular the trend of the d.o.f. in the 45° bending.

Of course the bending can start arbitrarily from any anchorage cross section maintaining the same characteristic.

In table 2 the manipulator parameters used for every simulation are reported. In table 3 the tendon tensions associated with the relative results are shown.

6.2. Fetching

When an octopus grasps some food, in order to fetch the food to the mouth, the arm generates a series of bends that serve as proximal, medial and distal joints [21] (figure 13).

To replicate this movement composed of three bends it is necessary to have at least three different anchorage cross sections. In the results below, two different fetch images are shown as example, performed with the model parameters of table 4 and the different actuation reported in table 5. The first fetching movement shown in figure 14 lies in one plane as the octopus one [21]. Since the actuation of the manipulator is not localized like the octopus muscles (all the tendons of the manipulator start from the base), the distal tendons can prevent the action of the more proximal ones if they are pulled in opposite directions.

Fetching in three dimensions has been investigated. The simulation results show that for our robot arm a three-dimensional fetching is more efficient; in fact with the same actuator strength the distal part of the arm is closer to the base (mouth) as shown in figure 15.

7. Conclusions

In conclusion, in this work a general geometrically exact steady-state model of an octopus-inspired robot arm driven by cables was developed. The ordinary differential equations that describe the behaviour of all the d.o.f. (deformation of the rod-like body) are fully reported. The model was experimentally validated and many interesting results are shown. It could be a powerful tool for mechanical design of such a manipulator because of its generality and because it includes the modelling of the tendon actuation. The model is developed following a continuum approach that leads to fast computation and the possibility to implement the model into the control algorithm.

The validation tests highlight a very small difference between the model and the real prototype (the average of the tip error is less than 6% of the total length of the arm) due to the nonlinearity of the material, the friction of the cables and in particular the human error in the manual extrapolation process of the midline from the pictures. This is an acceptable error compared to the benefit that arises from the approximations employed.

In the results it is shown how the model can be easily used to define important characteristics of such a system such as the selection of the bending plane and the best way to perform complex behaviours (e.g. fetching).

The model presented in this paper could be used for simulating the behaviour of many kinds of continuum soft robot arms composed of a slender body and driven by cables. Different shapes of the body could be tested as well as the effect of different paths of the tendons inside the robot body. There are no limitations to the position and number of anchorage cross sections that could be considered. Different materials could be tested too.

Furthermore, there are many reasons why the model represents a powerful tool for solving the control problem. It makes explicit the connection between the actuation and the configuration of the arm, which is not trivial like in the case of classical rigid body manipulators and is a fundamental lack in the state of the art. The numerical solution presented here is fast enough to implement the model on a microcontroller as virtual sensor or internal model. For those reasons the model presented in this paper is currently employed for the control of the octopus-inspired robot arm of section 3.

An important related work could be the investigation of the stiffness control of the robot arm in a dynamical environment (grasping object, in water current), which is a fundamental topic in modern control field. A robot arm such as that described in this paper is able to modulate its flexional stiffness in any configuration (if we neglect the longitudinal strain) just by properly actuating antagonistic tendons. Furthermore, the whole arm has to be considered as an end effector; therefore the relation between the curvatures of the grasped object and of the robot arm could play the role of the displacement difference of an impedance control. A deep investigation of these control properties will be carried out in a future work.

References

[1] Trivedi D, Rahn D C, Kier M W and Walker D I 2008 Soft robotics: biological inspiration, state of the art, and future research *Appl. Bionics Biomech.* **5** 99–117
[2] Laschi C, Mazzolai B, Mattoli V, Cianchetti M and Dario P 2009 Design of a biomimetic robotic octopus arm *Bioinspir. Biomim.* **4** 015006
[3] Webster R J III and Jones B A 2010 Design and kinematic modeling of constant curvature continuum robots: a review *Int. J. Robot. Res.* **29** 1661–83
[4] Cieslak R and Morecki A 1999 Elephant trunk type elastic manipulator—a tool for bulk and liquid type materials transportation *Robotica* **17** 11–16
[5] Hannan W and Walker D 2003 Kinematics and the implementation of an elephant's trunk manipulator and other continuum style robots *J. Robot. Syst.* **20** 45–63
[6] Kier W M and Stella M P 2007 The arrangement and function of octopus arm musculature and connective tissue *J. Morphol.* **268** 831–43
[7] Tatlicioglu E, Walker I D and Dawson D M 2007 New dynamic models for planar extensible continuum robot manipulators *Proc. IEEE/RSJ Int. Conf. on Intelligent Robots and Systems (San Diego, CA, USA)* pp 1485–90
[8] Camarillo D B, Milne C F, Carlson C R, Zinn M R and Salisbury J K 2008 Mechanics modeling of tendon-driven continuum manipulators *IEEE Trans. Robot.* **24** 1262–73
[9] Chirikjian G S and Burdick J W 1995 Kinematically optimal hyper-redundant manipulator configurations *IEEE Trans. Robot. Autom.* **11** 794–806
[10] Jones B A, Gray R L and Turlapati K 2009 Three dimensional statics for continuum robotics *Proc. IEEE/RSJ Int. Conf. on Intelligent Robots and Systems (St Louis, MO, USA)* pp 2659–64
[11] Boyer F, Porez M and Khalil W 2006 Macro-continuous computed torque algorithm for a three-dimensional eel-like robot *IEEE Trans. Robot.* **22** 763–75
[12] Zheng T, Branson D T, Guglielmino E and Caldwell D G 2011 A 3D dynamic model for continuum robots inspired by an octopus arm *Proc. IEEE/RSJ Int. Conf. on Intelligent Robots and Systems (Shanghai, China)* pp 3652–7
[13] Trivedi D, Lotfi A and Rahn C D 2008 Geometrically exact models for soft robotic manipulators *IEEE Trans. Robot.* **24** 773–80
[14] Antman S S 2005 *Nonlinear Problems of Elasticity* 2nd edn (*Applied Mathematical Sciences* vol 107) (New York: Springer)
[15] Struik D J 1961 *Lectures on Classical Differential Geometry* 2nd edn (New York: Dover)
[16] Simo J C 1985 A finite strain beam formulation. The three dimensional dynamic problem: part I *Comput. Methods Appl. Mech. Eng.* **49** 55–70

[17] Simo J C and Vu-Quoc L 1986 A three-dimensional finite-strain rod model: part II. Computational Aspects *Comput. Methods Appl. Mech. Eng.* **58** 79–116

[18] Simo J C and Vu-Quoc L 1988 On the dynamics of rods undergoing large motions—a geometrically exact approach *Comput. Methods Appl. Mech. Eng.* **66** 125–61

[19] Calisti M, Arienti A, Laschi C, Mazzolai B and Dario P 2010 Study and fabrication of bioinspired octopus arm mockups tested on a multipurpose platform *Proc. IEEE RAS & EMBS Int. Conf. on Biomedical Robotics and Biomechatronics (Tokyo, Japan)* pp 461–6

[20] Cianchetti M, Arienti A, Follador M, Mazzolai B, Dario P and Laschi C 2011 Design concept and validation of a robotic arm inspired by the octopus *Mater. Sci. Eng.* C **31** 1230–9

[21] Sumbre G, Fiorito G, Flash T and Hochner B 2006 Octopuses use a human-like strategy to control precise point-to-point arm movements *Curr. Biol.* **16** 767–72